High-Voltage Power-Line Conductor Anomaly Detection Using Magnetic Field

IEEE Sensors Council IEEE SENSORS JOURNAL, VOL. 26, NO. 13, 1 JULY 2026

High-Voltage Power-Line Conductor Anomaly Detection Using Magnetic Field

Francesco Messina, Emad Samuel Malki Ebeid, *Senior Member, IEEE*, and Marcello Chiaberge, *Member, IEEE*

***Abstract*—This article introduces a contactless, fully passive approach for locating faults in transmission-line conductors. The method relies on the magnetic fields generated by the line current and captures them using a low-cost, three-axis magnetic sensor integrated into a custom-designed drone payload. Unlike traditional inspection techniques, the proposed system performs rapid, multiposition magnetic scanning around the conductors within a short time window. By analyzing the spatial variations and temporal signatures of the measured magnetic field, the method can detect and characterize both external and internal anomalies, including potential structural degradations or irregular current distributions. Identified anomalies can be georeferenced accurately using the RTK-enabled GPS of the drone, allowing operators to determine their precise position along the transmission line. This capability supports targeted, close-range inspections and greatly enhances both the efficiency and safety of transmission-line maintenance activities. This article presents the experimental validation of the proposed method using a laboratory prototype. The prototype was tested on a 30-mm-diameter all-aluminum alloy conductor energized through a current transformer operating at 50 Hz and 350 A. These tests were designed to evaluate the system's ability to capture magnetic field signatures under realistic operating conditions, assess sensor performance, and verify the method's capability to detect and localize conductor anomalies in a repeatable, safe, and controlled environment.**

***Index Terms*—Anomaly detection, inspection uncrewed aerial vehicle (UAV) payload, low-cost magnetometer, magnetic field, power-line conductors.**

I. Introduction

HIGH-VOLTAGE transmission lines are among the most risk-sensitive assets in modern power systems, and their reliable operation is essential for supporting industry, communities, and critical services. These infrastructures comprise multiple components such as conductors, insulators, dampers, spacers, and towers. These components endure continuous exposure to harsh environmental conditions, including temperature fluctuations, wind loading, icing, and corrosion. Over years of service, this continuous exposure to external factors leads to aging, material degradation, and mechanical fatigue, necessitating periodic inspection to prevent emerging defects from developing into outages, wildfires, or catastrophic equipment failures.

Received 16 April 2026; accepted 6 May 2026. Date of publication 25 May 2026; date of current version 2 July 2026. The associate editor coordinating the review of this article and approving it for publication was Prof. Huang-Chen Lee. *(Corresponding author: Francesco Messina.)*

Francesco Messina and Marcello Chiaberge are with the Department of Electronics and Telecommunications (DET), PoliTo Interdepartmental Center for Service Robotics (PIC4SeR), Politecnico di Turin, 10129 Turin, Italy (e-mail: francesco_messina@polito.it; marcello.chiaberge@polito.it).

Emad Samuel Malki Ebeid is with the Maersk Mc-Kinney Moller Institute, SDU UAS Center, University of Southern Denmark, 5230 Odense, Denmark (e-mail: esme@sdu.dk).

Digital Object Identifier 10.1109/JSEN.2026.3694481

Although conventional inspection practices still rely heavily on ground patrols and costly manned helicopter surveys, uncrewed aerial vehicle (UAV)-based inspection has rapidly emerged as a safer, more efficient, and more scalable alternative. Most current drone-based inspection solutions, including those reported in [1], [2], [3], [4], [5], and [6] and many others, focus primarily on visible external damage like defects in insulators, spacer assemblies, or tower structures, using RGB, UV, thermal imaging, or LiDAR.

However, far fewer studies address faults occurring within the conductors themselves, despite the fact that conductors constitute a substantial portion of the total infrastructure. A study reported in [7] shows that conductor strands can suffer from cyclic mechanical loading, wind vibrations, corrosion, and manufacturing defects, which lead to fatigue and ultimately to strand fractures. Left unaddressed, such degradation can progress to internal or external strand fractures, compromising mechanical integrity and increasing the risk of a complete conductor break. Failures often originate from localized plastic deformation, oxidation, grain-structure weaknesses, or microcracking and can propagate rapidly under sustained tensile and vibratory loads. In severe cases, these hidden faults may culminate in conductor separation, posing immediate safety hazards and potentially causing widespread service outages.

Given these vulnerabilities, there is a growing need for innovative inspection techniques capable of detecting not only surface-visible defects but also internal strand anomalies that traditional optical methods may miss. This context underscores the importance of advancing sensing technologies, such as magnetic, eddy-current, or other noncontact methods, to enhance the monitoring and preventive maintenance of transmission-line conductors. The proposed magnetic field-based inspection framework offers several key advantages, some of which have also been highlighted in previous studies such as [8], [9], and [10].

1) The method leverages the magnetic field naturally generated by the line current, enabling safe inspection of energized conductors without external excitation, physical contact, or service interruption.
2) Since the magnetic field reflects the underlying current distribution, the approach is sensitive to both surface damage and hidden internal anomalies.
3) Distortions in the angular magnetic-field distribution allow the framework to localize anomalies around the conductor cross section and to qualitatively assess their severity based on the extent of the perturbation.

The approach is implemented using compact, low-cost three-axis anisotropic magneto resistance (AMR) magnetometers suitable for UAV integration and is experimentally validated under laboratory-controlled conditions. Furthermore, a scalable sensing and acquisition architecture is outlined to support automated, high-resolution inspection and future real-time drone-based deployment, offering operators a comprehensive overview of the scanned transmission line.

This article is organized as follows. Section II provides a detailed review of relevant literature, with emphasis on UAV-enabled monitoring technologies for power-line inspection and existing approaches for detecting power-line conductor anomalies. Section III reports the contributions of this work. Section IV presents the proposed methodology and laboratory validation setup. Section V discusses the experimental results and performances. Finally, Section VI summarizes the main findings and outlines directions for future research.

II. Literature Review

Automated inspection and diagnostic technologies for high-voltage power lines represent an urgent and necessary solution to ensure the reliability, safety, and long-term sustainability of rapidly expanding electrical networks. By overcoming the inherent limitations of traditional inspection methods, such as high operational risk, elevated costs, limited scalability, and inefficiencies, automated approaches enable more frequent, accurate, and proactive monitoring of critical infrastructure [11]. These advances are essential to support the growing demand for resilient power delivery while reducing maintenance burdens and enhancing overall grid performance.

A. Typical Anomalies and Damages

The newest diagnostic systems for this type of infrastructure are designed to identify a wide range of defects and anomalies [12], arising from the prolonged exposure of transmission components to harsh environmental and operational conditions. These defects are commonly classified according to the affected infrastructure element or to the nature of the anomaly, including electrical, thermal, mechanical, and environmental phenomena.

Insulators are among the most frequently inspected components, as they provide both mechanical support and electrical insulation. Typical defects, as reported in [4] and [5], include broken sheds, disks, or caps, particularly in porcelain insulators, often originating from thermal stress and mechanical loading. Polymeric insulators are susceptible to splits and punctures caused by material degradation, vandalism, or biological activity, potentially exposing internal metallic cores. Additional anomalies include surface aging, contamination, flashover, and corona discharges, which degrade insulation performance.

Conductors and transmission lines are critical to power delivery and are affected by both structural and environmental defects. As reported in [7] and [13], common issues include broken wires or strands caused by mechanical fatigue or extreme weather, which may lead to arcing, fires, or complete line failure. Internal corrosion in aluminum-conductor steel-reinforced (ACSR) conductors, such as zinc layer degradation on the steel core, is particularly challenging to detect using visual or thermal inspection and typically requires specialized techniques. Other reported defects include plastic deformation, excessive sagging, and structural degradation that compromise mechanical integrity and operational safety.

Towers and fittings provide structural support and protection for the transmission system and are subject to corrosion, mechanical fatigue, and component failure. Typical defects include corrosion of fasteners and sag adjusters, failure of vibration dampers, missing pins, and deterioration of connectors and spacers. Towers may also experience surface corrosion, partial deformation, or collapse due to environmental loads or external impacts.

Finally, corridor-level and specialized anomalies are often addressed using nonvisual sensing modalities. Vegetation encroachment within the transmission right-of-way poses a major safety risk and is commonly detected through clearance analysis using LiDAR or photogrammetry [6], [14].

Thermal anomalies, such as localized overheating, are identified through infrared imaging as in [11], while partial discharges and corona activity can be detected using ultraviolet sensors as presented in [1]. For example, Alam et al. [15] proposed a nonintrusive fault detection approach based on the excitation and sensing of electromagnetic surface waves propagating along the conductor. The authors introduce surface-wave launchers designed to be mounted directly on power cables. By injecting broadband high-frequency pulses and applying time-domain reflectometry (TDR), the system detects and localizes open-circuit faults based on reflections caused by impedance discontinuities.

These specialized diagnostic approaches complement visual inspection by revealing hidden electrical and thermal defects that are otherwise difficult to observe.

B. Platforms and Inspection Methods

Traditional inspection methods, such as manual ground-based visual or manned helicopter surveys, are highly labor-intensive, time-consuming, and inherently hazardous for operators. Moreover, they are often strongly dependent on human expertise, which limits their repeatability and accuracy. These limitations make conventional approaches particularly unsuitable for inspecting power-line infrastructure in complex, inaccessible, or remote environments, as explained in [13] and [14].

In this context, drone-based systems have become essential tools for modern infrastructure inspection, offering significant reductions in operational costs, inspection time, and human risk while improving data quality and coverage [1], [2]. They are increasingly employed for the surveillance and inspection of critical assets such as bridges, railways, and electrical transmission lines, particularly in environments that are difficult or unsafe for human operators to access [3].

Despite these advantages, limited flight time remains a key challenge for extended inspection missions. This constraint can be partially mitigated through the integration of recharging mechanisms. For example, a self-recharging drone platform has been proposed in [16] that exploits inductive energy harvesting from the magnetic field surrounding energized power lines, enabling the drone to recharge its battery while docked on the conductor. Experimental studies have shown that such systems significantly extend operational autonomy and enable long-duration inspection tasks.

Specialized inspection platforms have also been developed to operate directly on transmission-line conductors. For example, the work presented in [17] introduces an autonomous rover capable of traversing energized conductors, performing real-time visual inspections, detecting faults, and georeferencing their locations through onboard sensing and geo-tagging. Similarly, Barbosa [18] proposed a robotic module installed on overhead conductors and remotely operated from the ground via a radio link; the system employs eddy-current sensors to assess the remaining thickness of the zinc coating on steel strands, enabling the detection of internal corrosion.

Other contributions focus on infrastructure-based monitoring systems that measure electrical line parameters, with many approaches leveraging traveling-wave techniques for fault detection and localization [19], [20], [21], [22], [23], [24]. Additionally, the work of Silva et al. [25] presented a signal-processing-based approach combining wavelet transform and artificial neural networks, where fault detection is achieved by analyzing the energy of high-frequency wavelet coefficients in current signals to distinguish fault conditions from normal operating states.

Several studies have investigated the use of magnetic-field measurements for power-line monitoring and fault detection, exploiting the direct relationship between line current and the surrounding magnetic field. Kazim et al. [9] proposed a noncontact magnetic-sensor-based system for the rapid and accurate detection of short-circuit faults in electrical distribution networks. Their approach relies on highly sensitive and energy-efficient tunnel magnetoresistive (TMR) sensors installed on distribution poles without requiring service interruptions. By monitoring peak-to-peak magnetic-field variations, the system distinguishes between normal operating conditions, load imbalances, and short-circuit faults through comparison with predefined thresholds.

A different application of magnetic-field sensing is presented in [10], where a noninvasive technique for detecting and inspecting underground power cables is introduced. Magnetic-field measurements acquired at ground level are used to solve an inverse problem aimed at estimating both cable position and phase currents. This reconstruction process combines a least squares approximation (LSA) for current estimation with an artificial immune system (AIS) algorithm that iteratively optimizes the spatial coordinates of the conductors until the discrepancy between measured and modeled magnetic fields is minimized.

More recently, Ayambire [8] presented a high-precision, noncontact fault detection and localization method for transmission networks based on magnetic-field measurements. The proposed system employs arrays of magnetic sensors installed at transmission towers to capture the magnetic flux density associated with traveling waves generated during fault events. Relying on the Biot–Savart law, the method is validated through MATLAB/Simulink and ETAP simulations across multiple fault types.

In contrast to these approaches, the present work focuses on the analysis of cross-sectional angular magnetic-field distributions around a single conductor, with the objective of identifying localized current redistribution caused by internal or external conductor damage rather than detecting or localizing faults along the line. Moreover, the proposed framework is specifically designed for UAV-compatible inspection and emphasizes the use of low-cost sensors, geometric reconstruction of the magnetic field in the immediate vicinity of the conductor and provides intuitive visualization tools for anomaly detection. Unlike approaches that rely on distributed sensor networks permanently installed along the infrastructure, which can entail significant deployment, maintenance, and management costs, the proposed method avoids the need for fixed installations and is therefore more scalable for large-scale inspection campaigns. These distinctions position the proposed approach as a complementary magnetic field-based inspection strategy, particularly well-suited for noncontact, cross-sectional condition assessment of power conductors.

III. Contributions

The present work seeks to address a gap in current drone-based power-line inspection practices by introducing a robust, low-cost, and fully integrable inspection framework based on passive magnetic sensing. The main contributions of this work can be summarized as follows.

1) We introduce a fully passive, noncontact inspection methodology that exploits the magnetic field naturally generated by the line current to detect anomalies in energized power conductors, eliminating the need

for external excitation, physical contact, or service interruption.
2) We provide a first-order analytical model that explicitly relates localized conductor damage to current redistribution within the cross section and to measurable angular distortions of the external magnetic field, offering a physical interpretation of defect-induced magnetic signatures.
3) We propose a multiposition magnetic scanning approach that reconstructs the angular magnetic field distribution around the conductor cross section, enabling anomaly localization, qualitative assessment from visual magnetic-field maps, and normalized quantitative assessment through the newly introduced normalized angular distortion index (NADI) metric.
4) We experimentally validate the proposed framework on laboratory conductor samples with both internal and external artificial damages, demonstrating clear differentiation between healthy conditions, cut-type defects, and deformation-based anomalies.

IV. Methodology

The framework proposed in this work is designed to measure the magnetic field surrounding a section of the conductor using multiple magnetometers, enabling the detection of subtle variations in the electromagnetic signature of the line. By capturing the spatial distribution of the magnetic field from multiple points, the system aims to identify any local perturbations induced by internal or external anomalies within the cable structure. From a theoretical standpoint, the underlying principle relies on the fact that the magnetic field around a conductor is directly related to the distribution of the current density through Ampère's law and the Biot–Savart formulation. Under healthy operating conditions, the current in a stranded conductor is approximately symmetric across the cross section, resulting in a predictable and smooth magnetic field pattern. However, when the conductor develops physical alterations, such as broken strands, crushed regions, corrosion, induced thinning, or localized deformation, the electrical impedance of the affected zone changes. These changes in impedance force the current to redistribute itself, preferentially flowing through paths of lower resistive and inductive opposition. This redistribution disrupts both the magnitude and direction of the local current density. As a consequence, the magnetic field measured around the cable will deviate from its nominal profile. These deviations become measurable through multiposition magnetic scanning. By quantifying these perturbations, the framework enables noncontact, passive identification of internal and external faults that are otherwise difficult to spot with conventional inspections.

From a mathematical point of view, under the following initial assumptions: 1) magnetoquasistatic approximation at 50 Hz; 2) straight conductor and 2-D cross-sectional model; and 3) uniform current density J_0 in the healthy case. Maxwell–Ampère's law reduces to

$$\nabla \times \mathbf{B}(\mathbf{r}, t) = \mu_0 \mathbf{J}(\mathbf{r}, t). \tag{1}$$

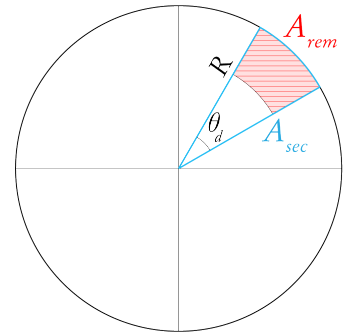

Fig. 1. Schematic of the cross section of the conductor with the damaged sector parameters used for the analytical model.

This formulation clearly explains the direct relation by which the magnetic field is determined by the cross-sectional distribution of the current density J. Therefore, any defect that alters conductivity or effective cross-sectional area modifies the current density and consequently produces a measurable distortion in the magnetic field B.

For a healthy conductor of radius R carrying rms current I, adopting the uniform current density approximation over the cross section, we have

$$J_0 = \frac{I}{\pi R^2} \tag{2}$$

which yields a classical axisymmetric field outside the conductor ($r > R$)

$$B_0(r) = \frac{\mu_0 I}{2\pi r}. \tag{3}$$

Equation 3 predicts no angular dependence in healthy conditions, so an almost perfect circular pattern is expected from experimental data for the healthy baseline. A localized defect, reflecting the type of artificial alterations introduced in the tested conductors, is modeled as a reduction of effective conductive area within a small angular sector θ_d of width $\Delta\theta$. The cross-sectional current density is represented by the piecewise angular model

$$J(\theta) = J_0\left[1 - \alpha\, \mathbf{1}_{\theta_d}(\theta)\right], \quad \theta \in [0, 2\pi) \tag{4}$$

where $\mathbf{1}_{\theta_d}(\theta)$ is 1 inside the damaged sector and 0 elsewhere and $\alpha \in [0, 1]$ is a severity factor. Referring to Fig. 1, let A_{rem} denote the area of removed material and let the geometric area of the sector be $A_{sec} = \pi R^2 \Delta\theta / 2\pi$. A first-order estimate is then given by

$$\alpha \approx \frac{A_{rem}}{A_{sec}}. \tag{5}$$

Equivalently, the defect induces a "missing" current

$$\Delta I \approx I \frac{A_{rem}}{\pi R^2} = I \frac{\Delta\theta}{2\pi} \alpha \tag{6}$$

which must redistribute through the remaining cross section, breaking angular symmetry and generating an anisotropic external magnetic field. To obtain a compact closed-form prediction of the angular distortion at the measurement radius r_s, we approximate the damaged sector as an equivalent negative line current $-\Delta I$ located at the conductor periphery along the damaged direction (radius R and angle θ_d). The total field is approximated as the superposition of: 1) the main line current I at the center and 2) the negative line current $-\Delta I$ at $r_d = R[cos\theta_d, sin\theta_d]$.

At a sensor location on a ring $r_s(\theta) = r_s[cos\theta, sin\theta]$, the magnitude of the perturbation due to the offset line current is

$$\Delta B(\theta) \approx \frac{\mu_0 \Delta I}{2\pi \rho(\theta)} \tag{7}$$

where

$$\rho(\theta) = \| r_s(\theta) - r_d \| = \sqrt{r_s^2 + R^2 - 2 r_s R \cos(\theta - \theta_d)}. \tag{8}$$

Thus, the total field magnitude on the measurement circle can be written as

$$B(\theta) \approx B_0(r_s) - \Delta B(\theta) \tag{9}$$

where the negative sign reflects the fact that the defect corresponds to a reduction of current in that sector (hence, opposite contribution to the nominal field direction). Equations 7 and 9 predict a localized angular perturbation centered at θ_d, whose amplitude scales with ΔI and whose spatial spread depends on (r_s, R). This provides a direct quantitative link between defect size (A_{rem}) and the measured angular distortion.

The proposed formulation represents a deliberately simplified analytical model and is not intended to provide exact quantitative predictions for real-world operating conditions. Its purpose is to offer a first-order physical interpretation that links conductor damage to current redistribution and the resulting magnetic-field distortions. To achieve this level of analytical tractability, several assumptions were introduced that may not fully hold in practical scenarios involving complex strand structures, material heterogeneity, environmental influences, and dynamic operating conditions. In practice, anomaly detection is fundamentally a data-driven problem. When the underlying physical system exhibits high complexity and a wide range of possible degradation mechanisms, constructing a comprehensive analytical model capable of describing all potential fault scenarios becomes impractical. Instead, data-driven strategies leverage the observation that healthy systems exhibit consistent and repeatable behavior, while anomalous conditions manifest as statistically significant deviations from this baseline.

A. Experimental Setup Equipment

In this section, we present the different components and instrumentation used throughout the experimental campaign.

The core of the system is the magnetometer module, implemented using the Adafruit breakout board equipped with the MMC5603NJ sensor, reported in Fig. 2. The MMC5603NJ is a highly integrated, monolithic three-axis AMR magnetic sensor featuring on-chip signal conditioning and a fully digital I^2C interface. It provides a full-scale measurement range of ± 30 Gauss, making it suitable for capturing both the nominal magnetic field produced by power-line currents and the small perturbations associated with conductor anomalies. Operating in its 20-bit high-resolution mode, the sensor achieves a sensitivity of 0.0625 mG per LSB, with a total rms noise level

Fig. 2. Adafruit breakout board equipped with the MMC5603NJ sensor.

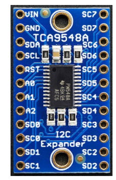

Fig. 3. TCA9548A multiplexer board.

of approximately 2 mG. This combination of high resolution, low noise, compact form factor ($25.4 \times 17.8 \times 4\, mm$), and low cost (under \$5) makes this magnetometer particularly well-suited as an initial choice for evaluating its potential as a drone-based inspection payload.

One limitation of this sensor is that each breakout board is manufactured with a fixed and nonconfigurable I^2C address, meaning that multiple units cannot coexist on the same bus. Since our experimental setup requires four sensors, it becomes necessary to introduce an I^2C TCA9548A multiplexer, reported in Fig. 3, which allows us to switch between channels sequentially.

The Uno R3 board, equipped with an ATmega328 microcontroller, was used to operate the four MMC5603NJ magnetometers through the I^2C multiplexer, running custom firmware.

For the experimental tests, we employed several 30-mm all-aluminum alloy conductor (AAAC) samples. Some conductors were kept in a healthy condition, while others were intentionally damaged, both externally and internally, to emulate realistic fault scenarios. Internal defects were introduced at known locations so that their magnetic signatures could later be compared with ground-truth references. For internal damage samples, defects were introduced by extracting the conductor core from the surrounding strands, applying a localized cut or hammer-type modification to the core, and subsequently reinserting it into the intact outer layers. During the reinsertion process, particular care was taken to preserve the original geometry and mechanical state of the conductor. The core strands were manually repositioned in their original configuration without applying additional mechanical stress or tension. The outer strands remained mechanically continuous and structurally intact throughout the procedure. The location and type of each defect were controlled during the preparation process, providing a known ground-truth reference even for internal damages. As a result, no additional deformation was introduced beyond the intended internal modification, ensuring that the observed magnetic-field variations are attributable to changes in the internal current-carrying paths rather than unintended mechanical effects. It should be noted that these artificial internal defects are not intended to reproduce the full morphology of strand failures developed in service. The defects introduced in this work were designed to provide perturbations of the internal current-carrying paths, allowing an initial assessment

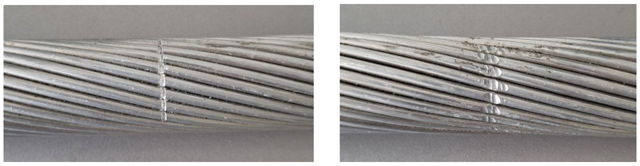

(a) (b)

Fig. 4. Examples of external damages induced in the conductor. (a) External cut damage. (b) External hammer damage.

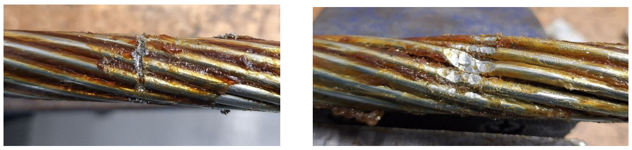

(a) (b)

Fig. 5. Examples of internal damages induced in the conductor. The visible dark/brown material corresponds to the neutral grease normally present between the internal layers of AAAC conductors and does not indicate oxidation or surface corrosion. (a) Internal cut damage. (b) Internal hammer damage.

of the sensitivity of the proposed magnetic inspection principle to internal conductive-path disturbances. Consequently, the measured signatures should be interpreted as proof-of-concept responses to artificially induced internal anomalies rather than exact replicas of real internal strand failures. Each conductor sample was energized using a current transformer configured to supply 350 A at 50 Hz with an output voltage of approximately 5 V, ensuring controlled, safe, and repeatable operating conditions for evaluating the proposed magnetic anomaly detection framework. Some examples of external and internal damaged cables are reported in Figs. 4 and 5.

To ensure stable and repeatable magnetic field measurements at different positions around the conductor, we designed a custom 3-D-printed modular sensing fixture. This device allows the four magnetometers to be mounted at precisely defined and interchangeable distances from the conductor surface, ensuring consistent sensor geometry across all tests. The modular design also facilitates rapid reconfiguration of sensor spacing and alignment. The 3-D model is shown in Fig. 6.

The fixture is designed so that, during data acquisition, it can be manually rotated by a predefined, fixed angle around the conductor while maintaining a constant axial position along its length. This enables the collection of multiple angular measurements at known orientations, effectively sampling the magnetic field in a full circumferential sweep. By combining the measurements obtained at each rotation step, the system can reconstruct the complete magnetic field distribution around the conductor's cross section, allowing us to analyze how different fault conditions modify the expected magnetic signature.

An example of the laboratory acquisition setup, featuring the conductor under test together with the 3-D-printed sensor fixture, is presented in Fig. 7.

B. Data Acquisition

A custom firmware was developed on the Uno microcontroller to manage the four MMC5603NJ magnetometers connected via an I^2C multiplexer. The code handles sensor

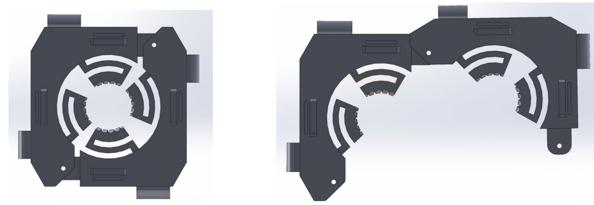

(a) (b)

Fig. 6. Custom 3-D-printed modular sensing fixture designed to hold and position the magnetometers at fixed distances around the conductor. (a) 3-D fixture module closed. (b) 3-D fixture module open.

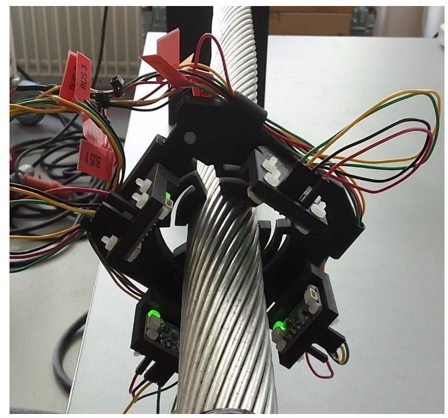

Fig. 7. Experimental setup for magnetic field acquisition around the conductor.

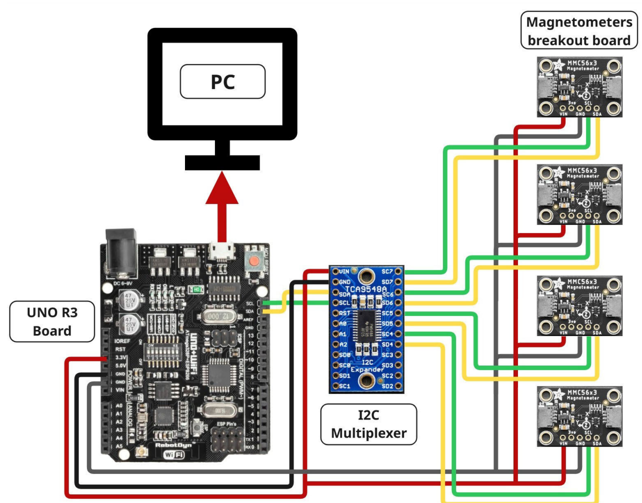

Fig. 8. Scheme of the complete data acquisition system showing sensor, multiplexer, and microcontroller connections.

configuration, calibration, timed sampling, and data streaming to a host computer. The connection scheme of the complete data acquisition system is reported in Fig. 8.

All four magnetometers share the same fixed I^2C address. To use them on a single bus, we connected each sensor to a separate channel of the I^2C multiplexer. The firmware selects the active sensor by writing to the multiplexer's control register; at any given time, only one sensor is connected to the microcontroller's I^2C bus.

For each sensor, at the start of the acquisition, the firmware performs: 1) a soft reset; 2) configuration of the output data rate (ODR) (nominally 1 kHz); 3) enabling continuous measurement mode; and 4) selection of high-power, 16-bit operation

These settings ensure that each MMC5603NJ continuously updates its three-axis magnetic field registers at a high and stable sampling rate. To compensate for sensor bias and residual magnetization, the code performs an automatic calibration routine for each sensor where the resulting three-axis offsets are stored in an array and also written in the microcontroller's EEPROM, so they persist across power cycles. During normal acquisition, these offsets are subtracted from the raw readings, providing bias-corrected magnetic field values.

Data acquisition is controlled by a timer that is configured to generate an interrupt at a fixed period, about 1.4 ms, corresponding to 700 Hz. The acquisition frequency was chosen as the highest rate that could be stably supported by the complete hardware–software chain. Higher rates introduced timing instabilities and duplicate samples due to sensor buffer limitations. Since the proposed method relies on consistent angular sampling, deterministic timing was prioritized over higher sampling rates. The selected frequency provides an effective balance between temporal resolution, measurement stability, and hardware reliability. On each timer interrupt, it reads from the magnetometer's data registers (X, Y, and Z high/low bytes) in a single burst.

Acquisition is performed sequentially, sensor by sensor, since a single I^2C bus is used. For the currently selected sensor, the system collects a fixed number of samples. Once the desired number of samples is reached, the firmware switches the multiplexer to the next sensor channel, resynchronizes to its data-ready status, and repeats the process. After all four sensors have been sampled, the acquisition run stops automatically.

This strategy provides time-stamped, bias-corrected magnetic field measurements from each sensor, sampled at a nearly uniform rate. Each measurement is packaged into a compact ASCII-hex data packet containing a packet identifier, the sensor index (multiplexer channel), the three corrected magnetic field components (X, Y, and Z in signed counts), and a 32-bit timestamp. These packets are streamed over the serial interface to a host computer, where they are logged and later processed for magnetic field reconstruction and anomaly detection.

For each acquisition, the fixture holds four sensors at mutually orthogonal (90°) positions around the conductor. By manually rotating the fixture 24 times in 15° steps, we obtain, for each sensor, a complete 360° sweep of the cable cross section. With the sensors located 25 mm from the cable center, this corresponds to sampling the magnetic field at angular intervals of about 6.5 mm of arc length along the cable circumference.

C. Data Processing

The raw magnetic data are stored as ASCII-hex log files, one for each of the 24 angular positions measured around the conductor. Every file contains a sequence of fixed-length packets that are decoded to retrieve the sensor identifiers, the three magnetic-field components, and their associated

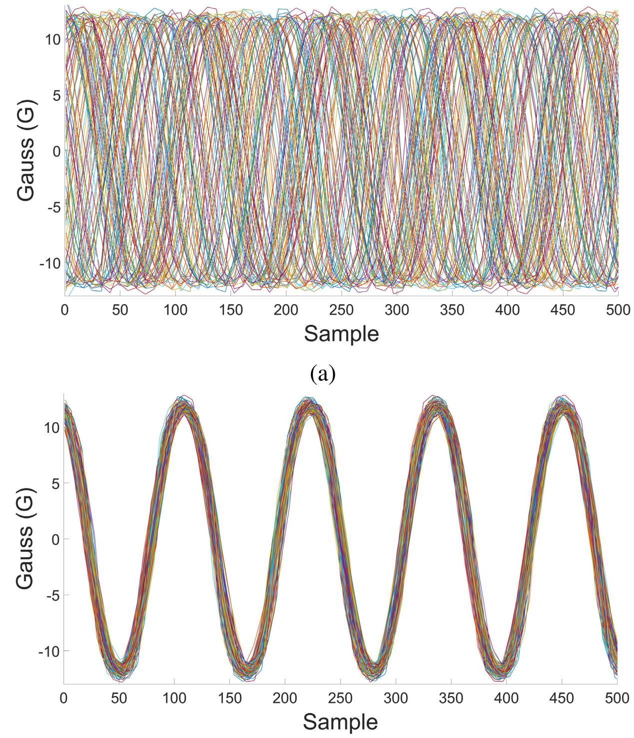

(a)

(b)

Fig. 9. Example of magnetic signals (a) before and (b) after synchronization, highlighting the effect of the data processing and alignment procedure.

timestamps. The raw values are then converted from counts into Gauss based on sensor specifications on the datasheet and the chosen resolution mode.

Because each measurement is acquired at a different time, the signals are not initially synchronized as can be seen in Fig. 9(a). To synchronize them, the first prominent crest of the selected axis is identified within an initial window for each signal, then these crest times are used to define a common start time and a shared analysis window corresponding to a fixed number of 50-Hz cycles. All signals are then resampled by linear interpolation onto a common, uniformly spaced time grid, so that they become directly comparable. Residual timing mismatches across positions are further corrected using cross correlation and signal-alignment routines, which estimate and compensate subsample time shifts. As a result, for each signal, we obtain a phase-aligned waveform segment describing the temporal evolution of the magnetic field at that location. The results of this process can be seen in Fig. 9(b). Since each of the 24 angular positions is measured by all sensors, the signals corresponding to the same position are averaged, providing a more robust estimate of the magnetic field at that location.

Anomalies can be identified either through visual inspection of the reconstructed magnetic-field cross sections or by quantitatively comparing statistical metrics, such as standard deviation and peak-to-peak amplitude, against a baseline obtained from healthy conductor samples.

V. Results

For the laboratory experiments, we classified the artificial defects into two main categories: cut damages and hammer damages, each representing a different failure scenario. Cut damages simulate the early stages of strand fracture, where one or more strands begin to separate due to fatigue or mechanical overload. Hammer damages, in contrast, emulate deformation-related faults in which the strand geometry is altered from its original circular shape, as might occur due to impact, compression, or severe bending.

To better reflect real-world operating conditions, each damage type was applied in two configurations: external, where the defect is visible on the outer surface of the conductor, and internal, where the damage is introduced beneath the external layer of strands. This distinction allows us to assess the system's ability to detect both surface-level anomalies and hidden defects that cannot be observed through conventional visual inspection.

To provide an intuitive visualization of the magnetic-field distribution, the processed measurements are mapped onto a 2-D representation of a cross section around the conductor. For each angular position, the known acquisition geometry, namely the conductor radius, the sensor distance, and the angular sampling step, is used to define the corresponding sensor location in polar coordinates.

For each frame, the discrete angular measurements acquired at the sensor radius are first interpolated along the circumferential direction to obtain a continuous angular magnetic-field profile. This profile is then visualized using a radial bar representation: for each angular direction, a bar originates at the conductor surface and extends radially outward, with its length proportional to the deviation of the local magnetic-field value from the frame-wise mean. By construction, bars reaching exactly the sensor radius correspond to angular positions where the magnetic field equals the mean value of the frame.

The bars are color-coded according to the magnetic-field magnitude, allowing both angular variations and relative intensity differences to be assessed simultaneously. Repeating this process for all time samples produces a time sequence of radial magnetic-field maps that can be interactively explored. This visualization emphasizes departures from an ideal, symmetric field distribution and provides an intuitive means to identify angular sectors where the magnetic response is consistently altered, potentially due to internal or external anomalies affecting the conductor.

An example of the behavior observed for a healthy cable is shown in Fig. 10. The black circle at the center denotes the conductor cross section, while the white smaller circles illustrate the geometric arrangement of the individual strands. In the case of a healthy conductor, the radial bars exhibit nearly uniform lengths and collectively form an approximately circular envelope, reflecting a homogeneous magnetic response around the cable.

Minor color variations may still appear at certain measurement points because the 24 angular scans are not acquired simultaneously, and so the current flowing inside the conductor exhibits natural fluctuations over time due to thermal effects on the conductor influenced by room temperature and air-conditioning cycles, leading to small cycle-to-cycle variations. Based on dedicated measurements, we estimate that

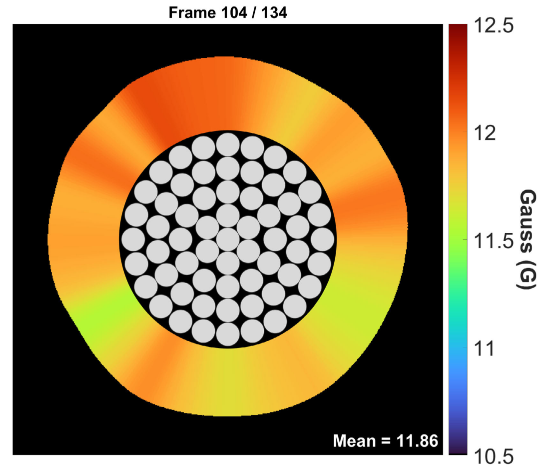

Fig. 10. Radial bar representation of the magnetic-field distribution around a healthy-cable cross section, showing a nearly uniform response.

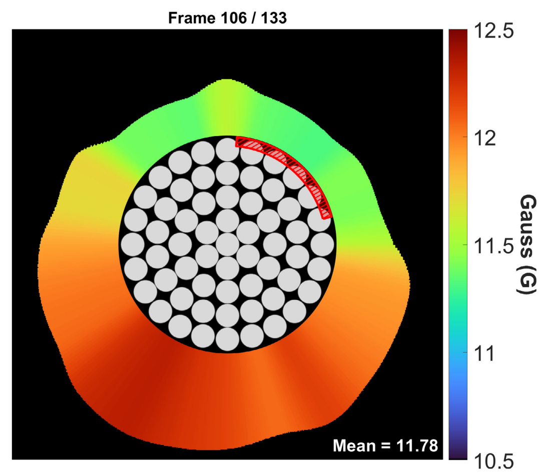

Fig. 11. Radial bar representation of the magnetic-field distribution in the presence of an external cut-type anomaly, whose location is highlighted by the striped red sector. This scan corresponds to the damage shown in Fig. 4(a).

the maximum fluctuations can be of 2 A, which can produce differences of about 0.1–0.2 Gauss between scans.

The results obtained from multiple test samples indicate that the two damage categories exhibit distinctly different behaviors. Cut-type defects, whether internal or external, produce a pronounced alteration of the magnetic field signature, with the magnitude of the disturbance increasing proportionally to the severity of the cut. Some examples of magnetic section anomalies are reported in Figs. 11 and 12.

In contrast, hammer-type deformations produce less pronounced deviations from the healthy magnetic-field behavior. While these variations may appear subtle in the reconstructed bar representations (Figs. 13 and 14), they remain detectable and quantifiable through statistical analysis of the acquired data. This behavior is consistent with the fact that hammer impacts primarily alter strand geometry without significantly disrupting current flow, whereas cut-type defects directly affect conductive paths and therefore generate stronger magnetic anomalies.

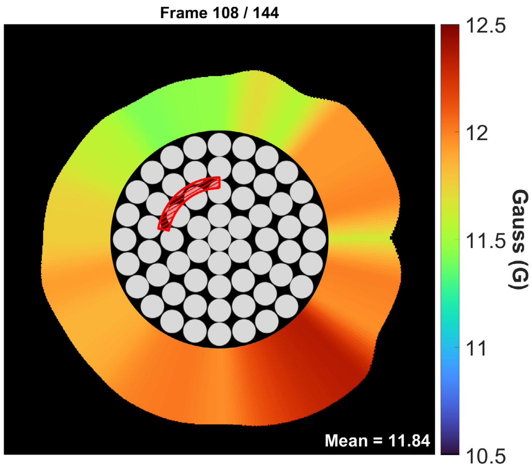

Fig. 12. Radial bar representation of the magnetic-field distribution in the presence of an internal cut-type anomaly, whose location is highlighted by the striped red sector. This scan corresponds to the damage shown in Fig. 5(a).

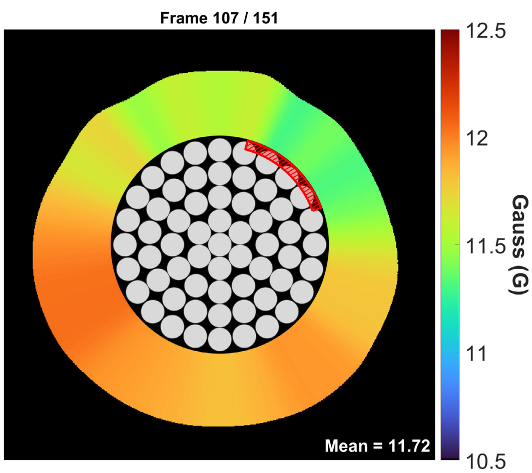

Fig. 13. Radial bar representation of the magnetic-field distribution in the presence of an external hammer-type anomaly, whose location is highlighted by the striped red sector. This scan corresponds to the damage shown in Fig. 4(b).

Beyond visual interpretation of the magnetic-field maps, anomalies can also be detected quantitatively through simple statistical measures. Both the standard deviation and the peak-to-peak amplitude of the magnetic signals exhibit marked departures from the values observed in the healthy-cable condition. Damaged sections consistently show increased variability and larger localized amplitude fluctuations, offering an objective and reliable indicator of abnormal behavior along the conductor. We have also introduced a quantitative metric referred to as the NADI. This index removes the dependence on the absolute current magnitude and enables comparison across different conductor geometries and sensor-to-conductor distances, providing an objective scalar measure to assess the condition of each scanned conductor section. This index metric is calculated as

$$NADI = \frac{\sigma_B}{\overline{B}} \tag{10}$$

where σ_B is the standard deviation and $\overline{B}$ is the magnetic field mean at that time instant.

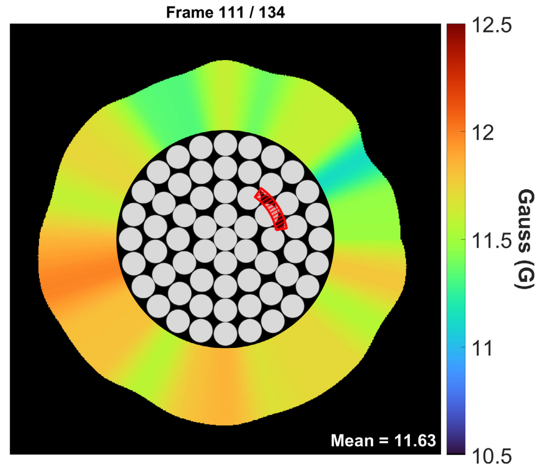

Fig. 14. Radial bar representation of the magnetic-field distribution in the presence of an internal hammer-type anomaly, whose location is highlighted by the striped red sector. This scan corresponds to the damage shown in Fig. 5(b).

TABLE I
STATISTICS SUMMARY OF REPORTED SCAN FRAMES

Damage Type	Damage Location	Std dev (Gauss)	Peak to Peak (Gauss)	NADI
Healthy	None	0.14	0.5	0.0118
Cut	External	0.35	1.048	0.0297
Cut	Internal	0.266	0.86	0.0225
Hammer	External	0.17	0.55	0.0145
Hammer	Internal	0.194	0.76	0.0167

TABLE II
STATISTICAL VARIABILITY OF THE REPORTED METRICS EVALUATED OVER 120 MEASUREMENTS (MEAN ± STANDARD DEVIATION)

Damage Type	Damage Location	Std dev (Gauss)	Peak to Peak (Gauss)	NADI
Healthy	None	0.16 ± 0.01	0.56 ± 0.06	0.013 ± 0.001
Cut	External	0.35 ± 0.01	1.08 ± 0.08	0.03 ± 0.001
Cut	Internal	0.262 ± 0.02	0.93 ± 0.08	0.022 ± 0.002
Hammer	External	0.21 ± 0.02	0.72 ± 0.09	0.018 ± 0.002
Hammer	Internal	0.23 ± 0.01	0.76 ± 0.05	0.02 ± 0.001

A summary of these statistics for the reported scan frames is provided in Table I. Table II reports the statistical variability of the metrics presented in Table I, evaluated over 120 measurements. These measurements were obtained from a single continuous acquisition by selecting the first 120 magnetic-field peaks. For each peak, the corresponding statistics were computed, after which the mean and standard deviation of each metric were calculated.

Based on the healthy reference dataset, consisting of 600 NADI values obtained from five separate measurements on healthy conductors, with 120 peak-based measurements extracted from each acquisition, the healthy NADI distribution was characterized empirically through its histogram, Fig. 15. The distribution was found to be strictly positive and

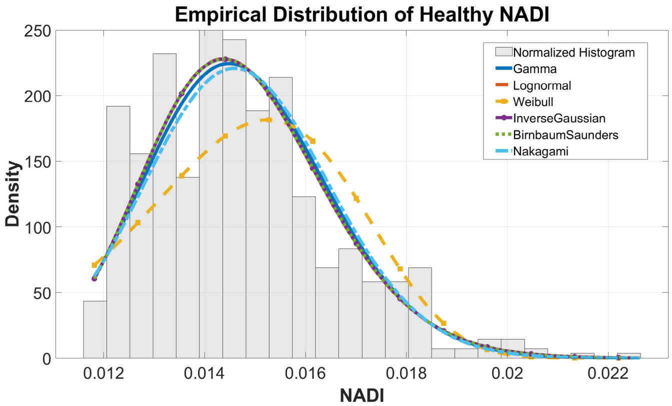

Fig. 15. Empirical distribution of healthy NADI values from the healthy reference dataset. The normalized histogram is shown together with the positive-support parametric distributions fit to the data.

mildly right-skewed. Anomaly reference levels were defined from the empirical percentile distribution of the healthy baseline. Specifically, a soft anomaly indication is associated with NADI values above the 95th percentile, while a hard anomaly indication is associated with $NADI$ values above the 99th percentile. For the healthy dataset analyzed here, these percentile-based reference levels are 0.01815 and 0.01999. These empirical reference levels are consistent with the observed separation between healthy and anomalous conditions, with cut-type defects exceeding the healthy baseline more clearly, while hammer-type defects produce weaker but still measurable deviations. These thresholds are intended as empirical reference limits for the present laboratory validation and not as definitive operational thresholds.

VI. Considerations for Field Deployment

Although the present study is limited to controlled laboratory conditions, several practical aspects must be considered for real-world deployment on energized transmission lines. In real high-voltage environments, additional effects such as electromagnetic interference, capacitive coupling, corona activity, and harmonic-rich currents may impact measurement robustness. These factors, however, do not alter the underlying physical principle of the proposed method and can be mitigated through established engineering solutions, including improved shielding, differential acquisition, isolation strategies, and higher sensitivity sensors. From an electromagnetic compatibility perspective, the sensing payload should also minimize susceptibility to electric-field coupling, common-mode interference, and cable-induced noise pickup.

The influence of harmonic-rich currents must also be considered. In a healthy conductor, harmonic components modify the temporal waveform of the magnetic field but do not inherently generate angular asymmetries in the reconstructed cross-sectional distribution. Therefore, the effectiveness of spatially resolved angular analysis is preserved.

From an industrial deployment perspective, several practical aspects must be addressed to enable UAV-based operation, including vibration-induced disturbances, sensor alignment stability, electromagnetic compatibility with onboard electronics, and reliable control of the sensor standoff distance from the conductor. While these challenges are nontrivial during free-flight operation, they can be substantially mitigated by adopting a docked inspection paradigm. In particular, performing magnetic field measurements while the UAV is physically docked onto the conductor, during recharging through an energy-harvesting mechanism, offers a robust solution to several of these constraints. As also suggested by the energy-harvesting and recharging approach discussed in [16], docked operation inherently suppresses flight-induced vibrations, ensures stable and repeatable sensor alignment, and guarantees a well-defined and constant sensor-to-conductor distance, all of which are critical for accurate and repeatable magnetic measurements. Moreover, the docking mechanism could incorporate a controlled mechanical pulley or guided translation system, enabling the UAV to move along the conductor at a constant and predefined velocity during the recharging phase. This would allow continuous scanning of the line while docked, combining improved measurement stability with extended inspection coverage.

Future developments will therefore focus on both sensor quality and system architecture. A key step will be the transition from sequential acquisition using four sensors to a circumferential array of 24 compact magnetometers capable of simultaneously capturing the full 360° magnetic-field cross section. This will eliminate temporal inconsistencies, improve spatial resolution, and significantly reduce sensitivity to environmental and current-related drift. To support this configuration, the sensing fixture will be redesigned as a fully plug-and-play payload, and the acquisition system will evolve from a microcontroller-based implementation to an FPGA-based architecture. The integration of docking and energy-harvesting mechanisms further enables in situ scanning during recharging phases, reducing operational downtime and extending inspection autonomy. Together, these developments pave the way toward a compact, robust, and scalable UAV-based inspection system suitable for real-world power-line monitoring.

From an operational perspective, the proposed architecture enables fast inspections; with an effective sampling rate of approximately 2.5 kHz, a 300-m line segment could be scanned at 1-cm longitudinal resolution in about 20 min.

VII. Conclusion

This study demonstrates the feasibility of passive near-field magnetic inspection of power conductors under controlled laboratory conditions. Measurements acquired with low-cost three-axis AMR magnetometers show that localized distortions in the magnetic-field distribution can be detected and angularly localized around the conductor cross section, enabling noncontact, data-driven condition assessment without service interruption.

Quantitatively, healthy conductors exhibited $NADI = 0.013 \pm 0.001$, whereas cut-type anomalies reached approximately 0.022 ± 0.002 for internal defects and up to about 0.030 ± 0.001 for external defects. The healthy baseline was characterized empirically using a reference dataset of 600 NADI values obtained from five separate measurements on healthy conductors, and the corresponding percentile distribution was used to derive empirical reference levels of 0.01815 and 0.01999 at the 95th and 99th percentiles, respectively. These results indicate clear separation for the most pronounced defect cases, confirm that the proposed framework is sensitive to both external and internal anomalies, and show that cut-type defects produce more pronounced magnetic distortions than hammer-type deformations, while hammer-type anomalies produce weaker but still measurable deviations, consistent with their lower impact on the current-carrying paths.

The experimental results also highlight current limitations. Environmental variability, sequential angular acquisition, and the performance constraints of low-cost magnetometers introduce measurement fluctuations that affect resolution and repeatability. Nevertheless, the adopted low-voltage, high-current setup remains representative of real transmission lines, as the external magnetic field at power frequency is primarily governed by line current rather than operating voltage, consistent with the magnetoquasistatic assumption.

At present, statistically robust operational thresholds for anomaly detection cannot yet be defined, as the investigated defects are artificially introduced and the current results are limited to controlled laboratory validation. Establishing reliable diagnostic criteria will require future studies on conductors extracted from real power lines, supported by high-resolution ground-truth inspection techniques. Moreover, the tested damages are simplified laboratory approximations and do not reproduce the full morphology and electromechanical boundary conditions of real conductor strand failures. Therefore, the observed magnetic-field distortions should be interpreted as proof-of-concept responses rather than exact replicas of real fatigue-induced strand-break signatures. Further validation on service-aged conductors, or on specimens produced through representative accelerated fatigue protocols, will be necessary to determine how closely the observed magnetic distortion patterns correspond to those generated by real fatigue-induced strand breaks.

Future work will focus on improving both the sensing hardware and the system architecture to support real-world deployment. In particular, the transition to a simultaneous 24-sensor circumferential array, together with a plug-and-play payload design, FPGA-based acquisition, and docked operation with energy harvesting, is expected to improve robustness, spatial resolution, and operational scalability for practical power-line inspection.

ACKNOWLEDGMENT

This work was carried out with the support of the Politecnico di Turin Interdepartmental Center for Service Robotics (PIC4SeR[1]) and the Digital and High-Frequency Electronics Section[2] at the University of Southern Denmark, Odense, Denmark, together with their members, during the research stay.

[1]https://pic4ser.polito.it/

[2]https://www.sdu.dk/en/forskning/sdu-digital-and-high-frequency-electronics

REFERENCES

[1] S. Kim, D. Kim, S. Jeong, J.-W. Ham, J.-K. Lee, and K.-Y. Oh, "Fault diagnosis of power transmission lines using a UAV-mounted smart inspection system," *IEEE Access*, vol. 8, pp. 149999–150009, 2020.

[2] H. Guan et al., "UAV-LiDAR aids automatic intelligent powerline inspection," *Int. J. Electr. Power Energy Syst.*, vol. 130, Sep. 2021, Art. no. 106987.

[3] R. H. Jacobsen et al., "Design of an autonomous cooperative drone swarm for inspections of safety critical infrastructure," *Appl. Sci.*, vol. 13, no. 3, p. 1256, Jan. 2023.

[4] Z. A. Siddiqui and U. Park, "A drone based transmission line components inspection system with deep learning technique," *Energies*, vol. 13, no. 13, p. 3348, Jun. 2020.

[5] B. Ge, C. Hou, Y. Liu, Z. Wang, and R. Wu, "Anomaly detection of power line insulator from aerial imagery with attribute self-supervised learning," *Int. J. Remote Sens.*, vol. 42, no. 23, pp. 8819–8839, Dec. 2021.

[6] Y. Zhang, X. Yuan, Y. Fang, and S. Chen, "UAV low altitude photogrammetry for power line inspection," *ISPRS Int. J. Geo-Information*, vol. 6, no. 1, p. 14, Jan. 2017.

[7] Y. Wang, Y. Guo, W. Liao, Y. Chen, W. Zhang, and Z. Zhang, "Fracture mechanisms and mechanical performance of aluminum conductor alloy reinforced wires in high-voltage transmission lines," *J. Mater. Eng. Perform.*, vol. 34, no. 16, pp. 18095–18109, Aug. 2025.

[8] P. N. Ayambire, "Magnetic sensor-based approach for overhead transmission lines fault detection and location using line fault current," *Turkish J. Electr. Power Energy Syst.*, vol. 5, no. 2, pp. 132–141, Jun. 2025.

[9] M. Kazim, A. H. Khawaja, U. Zabit, and Q. Huang, "Fault detection and localization for overhead 11-kV distribution lines with magnetic measurements," *IEEE Trans. Instrum. Meas.*, vol. 69, no. 5, pp. 2028–2038, May 2020.

[10] X. Sun, W. K. Lee, Y. Hou, and P. W. T. Pong, "Underground power cable detection and inspection technology based on magnetic field sensing at ground surface level," *IEEE Trans. Magn.*, vol. 50, no. 7, pp. 1–5, Jul. 2014.

[11] L. Yang, J. Fan, Y. Liu, E. Li, J. Peng, and Z. Liang, "A review on state-of-the-art power line inspection techniques," *IEEE Trans. Instrum. Meas.*, vol. 69, no. 12, pp. 9350–9365, Dec. 2020.

[12] X. Liu, X. Miao, H. Jiang, and J. Chen, "Data analysis in visual power line inspection: An in-depth review of deep learning for component detection and fault diagnosis," *Annu. Rev. Control*, vol. 50, pp. 253–277, Jun. 2020.

[13] C. Liao et al., "Detecting broken strands in transmission lines based on pulsed eddy current," *Metals*, vol. 12, no. 6, p. 1014, Jun. 2022.

[14] C. Chen, B. Yang, S. Song, X. Peng, and R. Huang, "Automatic clearance anomaly detection for transmission line corridors utilizing UAV-borne LiDAR data," *Remote Sens.*, vol. 10, no. 4, p. 613, Apr. 2018.

[15] M. N. Alam, R. H. Bhuiyan, R. A. Dougal, and M. Ali, "Design and application of surface wave sensors for nonintrusive power line fault detection," *IEEE Sensors J.*, vol. 13, no. 1, pp. 339–347, Jan. 2013.

[16] D. Stuhne et al., "Design of a wireless drone recharging station and a special robot end effector for installation on a power line," *IEEE Access*, vol. 10, pp. 88719–88737, 2022.

[17] P. S. Ranaweera, D. C. Alahakoon, K. S. S. Prabhashwara, and A. M. G. V. I. Lakmal, "Autonomous transmission line inspection and fault detection system," in *Proc. Moratuwa Eng. Res. Conf. (MERCon)*, May 2018, pp. 402–407.

[18] C. F. Barbosa, "An eddy current sensor for conductor inspection on energized power lines," in *Proc. 3rd Int. Conf. Appl. Robot. Power Ind.*, Foz do Iguassu, Brazil, Oct. 2014, pp. 1–5.

[19] J. Ding, X. Wang, Y. Zheng, and L. Li, "Distributed traveling-wave-based fault-location algorithm embedded in multiterminal transmission lines," *IEEE Trans. Power Del.*, vol. 33, no. 6, pp. 3045–3054, Dec. 2018.

[20] J. A. De Oliveira Neto, C. A. F. Sartori, and G. M. Junior, "Fault location in overhead transmission lines based on magnetic signatures and on the extended Kalman filter," *IEEE Access*, vol. 9, pp. 15259–15270, 2021.

[21] A. Ghaderi, H. A. Mohammadpour, and H. Ginn, "Active fault location in distribution network using time-frequency reflectometry," in *Proc. IEEE Power Energy Conf. at Illinois (PECI)*, Feb. 2015, pp. 1–7.

[22] S. Lin, Z. Y. He, X. P. Li, and Q. Q. Qian, "Travelling wave time-frequency characteristic-based fault location method for transmission lines," *IET Gener., Transmiss. Distrib.*, vol. 6, no. 8, pp. 764–772, Aug. 2012.

[23] M. K. Ngwenyama, P. F. L. Roux, and L. J. Ngoma, "Traveling wave fault location detection technique for high voltage transmission lines," in *Proc. 2nd Int. Conf. Emerg. Technol. (INCET)*, May 2021, pp. 1–7.

[24] M. Hudomalj, A. Trost, and A. Campa, "Traveling wave method for event localization and characterization of power transmission lines," *Electric Power Syst. Res.*, vol. 232, Jul. 2024, Art. no. 110382.

[25] K. M. Silva, B. A. Souza, and N. S. D. Brito, "Fault detection and classification in transmission lines based on wavelet transform and ANN," *IEEE Trans. Power Del.*, vol. 21, no. 4, pp. 2058–2063, Oct. 2006.

Francesco Messina received the B.S. degree in mechanical engineering and the M.S. degree in mechatronic engineering from Politecnico di Turin, Turin, Italy, in 2018 and 2020, respectively.

He is currently a Ph.D. Fellow with the Department of Electronics and Telecommunications, Politecnico di Turin. His research interests include anomaly detection, perception for UAVs, computer vision, photogrammetry, and thermal/hyperspectral imaging, which he brings together in his research in drone-based inspection and monitoring applications.

Emad Samuel Malki Ebeid (Senior Member, IEEE) received the Ph.D. degree in distributed embedded systems from the University of Verona, Verona, Italy, in 2014, with a European doctorate label.

He is a Professor and the Head of the Digital and High-Frequency Electronics Section, University of Southern Denmark, Odense, Denmark. He has published more than 80 papers in leading journals and flagship conferences in robotics and embedded systems, and serves as the Coordinator of several large-scale national and European projects, including EUDP Robots4Green, EU H2020 Drones4Safety, and Innovation Fund Denmark Grand Solutions Drones4Energy. His research focuses on autonomous drone systems for powerline inspection, interaction, and recharging, using advanced reconfigurable embedded platforms based on MPSoCs and FPGAs to enable real-time sensing, control, and energy-aware operation.

Dr. Ebeid was a recipient of the Prestigious Carlsberg Semper Ardens Accomplish Grant for the FreeFly Project.

Marcello Chiaberge (Member, IEEE) is currently an Associate Professor with the Department of Electronics and Telecommunications, Politecnico di Turin, Turin, Italy. He is also the Co-Director of the Mechatronics Lab, Politecnico di Turin, and the Director and a Principal Investigator of the Interdepartmental Center for Service Robotics (PIC4SeR), Turin. He has authored more than 100 articles accepted in international conferences and journals, and he is the co-author of nine international patents. His research interests include hardware implementation of neural networks and fuzzy systems, and the design and implementation of reconfigurable real-time computing architectures.

Open Access funding provided by 'Politecnico di Torino' within the CRUI CARE Agreement